Analysis of HO_2 and OH Formation Mechanisms Using FM and UV Spectroscopy in Dimethyl Ether Oxidation[†]

Kotaro Suzaki,[*,‡] Kentaro Tsuchiya,[§] Mitsuo Koshi,[||] and Atsumu Tezaki[⊥]

Departments of Mechanical Engineering and Chemical Engineering, School of Engineering, The University of Tokyo, Hongo 7-3-1, Bunkyo-ku, Tokyo 113-8656, Japan, National Institute of Advanced Industrial Science and Technology (AIST), Onogawa 16-1, Tsukuba, Ibaraki, 305-8569, Japan, and Graduate School of Science and Engineering, Toyama University, 3190 Gofuku, Toyama, 930-8555, Japan

Received: November 17, 2006; In Final Form: February 4, 2007

Product formation pathways in the photolytically initiated oxidation of CH_3OCH_3 have been investigated as a function of temperature (298−600 K) and pressure (20−90 Torr) through the detection of HO_2 and OH using Near-infrared frequency modulation spectroscopy, as well as the detection of $CH_3OCH_2O_2$ using UV absorption spectroscopy. The reaction was initiated by pulsed photolysis with a mixture of Cl_2, O_2, and CH_3OCH_3. The HO_2 and OH yield is obtained by comparison with an established reference mixture, including CH_3OH. The $CH_3OCH_2O_2$ yield is also obtained through the procedure of estimating the $CH_3OCH_2O_2/HO_2$ ratio from their UV absorption. A notable finding is that the OH yield is 1 order of magnitude larger than those known in C_2 and C_3 alkanes, increasing from 10% to 40% with increasing temperature. The HO_2 yield increases gradually until 500 K and sharply up to 40% over 500 K. The $CH_3OCH_2O_2$ profile has a prompt rise, followed by a gradual decay whose time constant is consistent with slow HO_2 formation. To predict species profiles and yields, simple chlorine-initiated oxidation model of DME under low-pressure condition was constructed based on the existing model and the new reaction pathways, which were derived from this study. To model rapid OH formation, OH direct formation from $CH_3OCH_2 + O_2$ was required. We have also proposed that a new HCO formation pathway via QOOH isomerization to HOQO species and $OH + CH_3OCH_2O_2 \rightarrow HO_2 + CH_3OCH_2O$ are to be considered, to account for the fast and slow HO_2 formations, as well as the total yield. The constructed model including these new pathways has successfully predicted experimental results throughout the entire temperature and pressure ranges investigated. It was revealed that the HO_2 formation mechanism changes at 500 K, i.e., $HCO + O_2$ via $HCHO + OH$ and the above proposed direct HCO formation dominates over 500 K, while a series of reactions following $CH_3OCH_2O_2$ self-reaction and $OH + CH_3OCH_2O_2$ reaction mainly contribute below 500 K. The pressure dependent rate constant of the CH_3OCH_2 thermal decomposition reaction has been separately measured since it has large negative sensitivity for HO_2 formation and is essential to eliminate the ambiguity in the $CH_3OCH_2 + O_2$ mechanism at higher temperature.

Introduction

The chemical kinetic mechanism of hydrocarbon autoignition has attracted much attention, not only by combustion chemists but also automobile engineers who seek to settle engine knocking and to actualize an alternative engine technology such as HCCI (homogeneous charge compression ignition).[1] The reactions of hydrocarbons with molecular oxygen are particularly important in low temperature (500 K < T < 1000 K) combustion, which governs autoignition features such as multistage ignition and negative temperature coefficient (NTC) behaviors. Through experimental studies consisting of time-resolved or indirect product analysis in thermal and photolysis reactors, as well as theoretical studies, the general description of this reaction has been established,[2−4] as described below.

An alkyl radical (R) formed through hydrogen abstraction by active radicals like OH reacts with the molecular oxygen to form the alkylperoxy radicals (RO_2):

$$R + O_2\,(+M) \rightarrow RO_2\,(+M) \tag{1}$$

As the RO_2 is stable at temperatures lower than that of low-temperature combustion, RO_2−RO_2 self-reaction and reactions with other species like NO_x is important in atmospheric chemistry.[5] At higher temperatures the RO_2 may isomerize via hydrogen transfer to form a hydroperoxy alkyl radical (QOOH);

$$RO_2\,(+M) \rightarrow QOOH\,(+M) \tag{2}$$

This isomerization reaction occurs through a ring structure transition state (TS) and the six-membered ring TS is least strained; therefore, the rate depends on the position of hydrogen relative to the OOH site.

The QOOH species decomposes to form OH and HO_2 or reacts with O_2;

[†] Part of the special issue "James A. Miller Festschrift".

[*] Corresponding author. Present address: Environment Research Department, National Traffic Safety and Environment Laboratory, Postal address; 7-42-27, Jindaiji-Higashimachi, Chofu, Tokyo, Japan, 182-0012. Telephone +81-422-41-3220, Fax: +81-422-76-8604, E-mail: suzaki@ntsel.go.jp.

[‡] Department of Mechanical Engineering, School of Engineering, The University of Tokyo.

[§] National Institute of Advanced Industrial Science and Technology (AIST).

[||] Department of Chemical Engineering, School of Engineering, The University of Tokyo.

[⊥] Graduate School of Science and Engineering, Toyama University.

10.1021/jp067646j CCC: $37.00
Published on Web 04/25/2007

$$\text{QOOH} \rightarrow \text{O-heterocycle} + \text{OH} \quad (3)$$

$$\text{QOOH} \rightarrow \text{alkene} + \text{HO}_2 \quad (4)$$

$$\text{QOOH} + \text{O}_2 \leftrightarrow \text{O}_2\text{QOOH} \quad (5)$$

At the condition of excess O_2 concentration or higher pressure, the second O_2 addition reaction may dominate in the QOOH reaction system. As the O_2QOOH species finally produces two OH and one alkoxy radical (RO), the growing chain reaction system is established. The decomposition reactions 3 and 4 become dominant as the temperature increases. While the OH forming reaction 3 is a chain propagation step, reaction 4 is a chain termination step owing to the formation of HO_2, which is relatively inactive in the range of low-temperature oxidation. Consequently, the branching ratio between reactions 3 and 4 is an essential part determining the NTC character of individual hydrocarbons.

Taatjes and co-workers have provided further insights on the R + O_2 reactions through direct time-resolved measurements of HO_2 and OH, and RRKM-master equation calculations.[6−15] Their notable finding is the direct HO_2 and OH formation, distinguished from the slow formation reactions via stabilized RO_2 in C_2H_5 + O_2 and C_3H_7 + O_2 reactions.[7,8,13,14]

$$\text{R} + \text{O}_2 \rightarrow \text{alkene} + \text{HO}_2 \quad (6)$$

$$\text{R} + \text{O}_2 \rightarrow \text{O-heterocycle} + \text{OH} \quad (7)$$

In the reactions of ethyl and propyl with molecular oxygen, the HO_2 yield gradually increases with increasing temperature in the range 296−550 K and drastically increases above 550 K. On the other hand, OH formation is insignificant throughout the entire temperature range. This is because either isomerization to QOOH or QOOH decomposition has a higher barrier than that of HO_2 elimination from RO_2.[13] Substantial participation of QOOH and OH formation is expected in butyl and larger alkyls and, in practice, the reduction of HO_2 yield was recognized in their butane experiment.[10] They also confirmed HO_2 formation in the reaction of the neopentyl radical with molecular oxygen, despite the fact that the formation of the conjugate alkene + HO_2 is structurally impossible.[11] As RO_2 isomerization and OH formation from QOOH decomposition is feasible, which is supported by their OH detection and detailed quantum chemical calculations,[16] they proposed that the HO_2 is formed secondarily by the reaction RO_2 + OH.

Dimethyl ether (CH_3OCH_3: DME) is proposed as an alternative fuel for diesel engines. Besides the high ignitability, denoted by the cetane number of 55−60, this oxygenated hydrocarbon without a C−C bond has the distinguishing advantage of soot free combustion. While the ignition character of DME has two stages and NTC behavior like *n*-heptane, the simple structure enables us to reveal the detailed chemical mechanism.

The DME oxidation mechanism has been examined by shock tubes, rapid compression machines, flow reactors and burners.[17−29] Detailed chemical kinetics models were proposed by Dagaut et al.[17] and by Curran et al.[19] In 2000, Curran et al. modified the DME oxidation model from the point of formic acid (HCOOH) formation.[21,22] In these kinetic models, the low-temperature oxidation mechanism of DME is the simplest form of the above-mentioned general hydrocarbon oxidation, in which there is no branching to isomers.

$$\text{CH}_3\text{OCH}_3 + \text{O}_2 \text{ or OH} \rightarrow \text{CH}_3\text{OCH}_2 + \text{HO}_2 \text{ or H}_2\text{O} \quad (8)$$

$$\text{CH}_3\text{OCH}_2 + \text{O}_2\ (+\text{M}) \rightarrow \text{CH}_3\text{OCH}_2\text{O}_2\ (+\text{M}) \quad (9)$$

$$\text{CH}_3\text{OCH}_2\text{O}_2\ (+\text{M}) \rightarrow \text{CH}_2\text{OCH}_2\text{O}_2\text{H}\ (+\text{M}) \quad (10)$$

$$\text{CH}_2\text{OCH}_2\text{O}_2\text{H}\ (+\text{M}) \rightarrow \text{OH} + 2\text{HCHO}\ (+\text{M}) \quad (11)$$

As the isomerization reaction (10) has a six-membered ring transition state and the barrier height of both reactions 10 and 11 is lower than the energy level of R + O_2 reactants, OH formation is more favorable than that of C_2H_5 + O_2.

This reaction mechanism was supported by several elementary kinetics studies[30−38] using UV absorption, FTIR, and mass-spectrometric sampling. Sehested et al. investigated the reaction mechanism of the CH_3OCH_2 + O_2 reaction at 296 K and 0.38 − 940 Torr using FTIR.[32] They found that at the lowest pressure condition, the HCHO yield reaches approximately 200%. This indicates that reactions 9−11 occur kinetically as one step when stabilization by a third body is avoided at this low pressure. At higher pressure, methyl formate (CH_3OCHO) and methyl hydroperoxy (CH_3OCH_2OH), which are secondary products of once stabilized $CH_3OCH_2O_2$, are dominant. Rosado-Reyes et al.[38] examined the CH_3OCH_2 + O_2 reaction mechanism, detecting HCHO, CH_3OCHO, and HCOOH with time-resolved IR absorption techniques in the temperature range 295−600 K and the pressure range 20−200 Torr, where the HCHO yield increases and CH_3OCHO decreases with increasing temperature. This indicates that while at lower temperature the CH_3OCHO is mainly formed via a series of $CH_3OCH_2O_2$ self-reactions, at higher temperature the $CH_3OCH_2O_2$ decomposes to mainly form HCHO. Theoretical calculations were conducted by Yamada et al. and Andersen et al.[35−37] These studies generally support the dominance of OH formation.

In our previous study, the HO_2 formation pathway between 550 and 600 K in the reaction CH_3OCH_2 + O_2 was investigated by detecting HO_2 and OH with the same procedure as developed by Taatjes et al.[39] It was argued that HO_2 is mainly formed by the reaction OH + HCHO, a part of which is formed promptly via the sequence without stabilization. We also detected $CH_3OCH_2O_2$ and CH_3OCH_2 radicals with the UV absorption technique in the same cell between 298 and 600 K.[40] By modifying the mechanism indicated in the Rosado-Reyes et al. paper, we proposed a different mechanism of HO_2 formation at room temperature from that at 600 K.

In this paper, we describe the experimental and analytical procedures conducted in the temperature range 298−625 K and the pressure range 20−90 Torr in more detail to further discuss and give confidence to the proposed mechanism. Another pathway contributing to HO_2 formation, i.e., HCO formation via QOOH isomerization was also included in our model. Since this is not considered in previous theoretical studies, our own quantum chemical calculations are also conducted to further validate the reaction mechanism.

Experimental Methods

To examine the HO_2 formation in the reaction of CH_3OCH_2 + O_2, OH and $CH_3OCH_2O_2$ were also detected using the NIR−FM and UV absorption techniques, besides HO_2 detection. The reaction is initiated by pulsed photolysis in a mixture of Cl_2, O_2 and DME with He buffer to establish the following reaction sequence:

$$Cl_2 + h\nu \rightarrow 2Cl \qquad (12)$$

$$Cl + CH_3OCH_3 \rightarrow HCl + CH_3OCH_2 \qquad (13)$$

$$CH_3OCH_2 + O_2 \rightarrow \text{products} \qquad (14)$$

Initial [DME]/[Cl] and $[O_2]/[Cl_2]$ are maintained larger than 60 to ensure prompt completion of reaction 13 and 100% yield of reaction 14 to $[Cl]_0$ by avoiding CH_3OCH_2 + Cl and CH_3OCH_2 + Cl_2 reactions. The yield of HO_2 relative to the initial Cl concentration in the reaction of $CH_3OCH_2 + O_2$ was determined by comparison with the reference reaction of $CH_2OH + O_2$ from a sample of CH_3OH;

$$Cl + CH_3OH \rightarrow HCl + CH_2OH \qquad (15)$$

$$CH_2OH + O_2 \rightarrow HO_2 + HCHO \qquad (16)$$

To determine the OH yield compared with the initial Cl concentration in the reaction of $CH_3OCH_2 + O_2$, the OH signals from this reaction were also compared with those from the reference reaction. The OH reference was obtained by adding NO to the HO_2 reference mixtures, where

$$HO_2 + NO \rightarrow OH + NO_2 \qquad (17)$$

takes place. A typical condition was $[Cl_2] = 2 \times 10^{14}$, $[O_2] = 1.2 \times 10^{16}$, $[DME] = [CH_3OH] = 1 \times 10^{15}$, and total gas density $= 1.1 \times 10^{18}$, all in molecules cm^{-3}, where the concentration is varied on purpose, as described later. The photolysis yield of the Cl atom is estimated as ca. 5% of Cl_2 at the typical 355 nm fluence of about 110 mJ/cm^2. Pressure was controlled according to temperature changes between 298 and 625 K, so as to maintain a constant total density, except for pressure dependent measurements. The photolysis repetition rate was set at 1 Hz to meet with the mean gas residence time at a typical flow rate of 5200 N-cm^3/min. Usually the time-resolved signals were averaged over 1000 times in a digital oscilloscope.

a. NIR Detection. HO_2 and OH were detected in this method. The experimental setup using FMS with a Herriott type multipass cell was originally developed to detect HO_2 by Taatjes and co-workers.[41] Our apparatus in the part of FMS with a multipass cell has been described in detail elsewhere.[42] The UV absorption function was added to our FMS setup. The schematic of the experimental system is shown in Figure 1. The components of FMS and the multipass cell are described briefly here. A CW diode laser, tunable between 6900 and 7090 cm^{-1} (1410−1450 nm), (New Focus, Velocity 6327) is used as the probe light source. The output of the diode laser is two-tone frequency modulated at 599.8 ± 2.6 MHz through an EOM (New Focus 4423M). The beam is then collimated, introduced into a Herriott type multipass cell, and finally fed into a photoreceiver (New Focus 1811MFS). The photoreceiver output signal is demodulated to an FM signal by mixing with a frequency-doubled fraction of the 2.6 MHz modulation signal and low-pass filtering. The signal is averaged with an oscilloscope (Tektronix TDS 520A) and stored in a PC. A partially reflected beam is introduced in a wavemeter (Burleigh WA-1500) for continuous monitoring of the wavelength. The Herriott cell consists of two concave mirrors placed coaxially at a distance of 1.5 m, between which a light path of 12 reflections at each mirror was established for this study. The center region of about 60 cm between two mirrors is the observation region where the probe beam is overlapped with the photolysis beam from a frequency tripled Nd:YAG laser (Continuum Surelite 2) passed through center holes of the Herriott mirrors, hence the effective absorption length is approximately 15 m. The cell is wrapped by a set of electric heaters, and three-zone temperature control is conducted so that the overlapped region is well within the flat temperature zone.

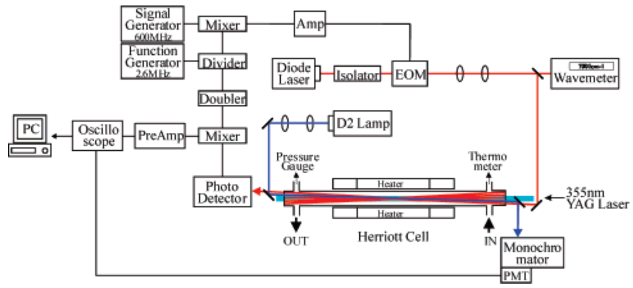

Figure 1. Experimental apparatus of flash/photolysis time-resolved near-IR frequency modulation spectroscopy, combined with UV absorption spectroscopy. The NIR beam undergoes 23 reflections in the Herriott type cell, and UV light is transmitted through a single path in the same cell.

In our study, HO_2 was detected in the first electronic transition at 1.4 μm, whereas the band detected by Taatjes et al. is mainly the O−H vibrational overtone at 1.5 μm. The 1.4 μm band has a clear rotational structure in the $(000)'-(000)''$ envelope, as analyzed by the high-resolution emission spectroscopic study of Fink and Ramsay,[43] and most of the lines are separable with the current resolution. A potential merit of the 1.4 μm band is selective detection of DO_2,[44] OH,[45] H_2O_2[42] in a narrow range of wavelengths using a high-resolution diode laser. Figure 2 shows (a) HO_2, (b) DO_2, and (c) OH spectra using FMS with the 1.4 μm diode laser at 298 K, though DO_2 detection is not currently an issue. In this study, HO_2 was detected at 7013.520 cm^{-1} of the A-X $(0'-0'')^{1-0}Q_2(18)$ transition[43] and OH was detected at 6971.291 cm^{-1} of $Q_{1e}(1.5)$ of the vibrational overtone.[45]

b. UV Detection. The absorption setup was established in the Herriott type cell without affecting NIR−FM function. A 30 W deuterium lamp (Hamamatsu, L7296−50) was employed as a light source. The UV light was collimated, and fed into the cell through the slits in the Herriott concave mirrors placed for the NIR beam passage. The UV light was transmitted directly through the cell without reflection in the Herriott mirrors. A pair of dichroic mirrors (99% reflection in 210−280 nm and 99% transmission in 1410−1450 nm) were used to mix and separate the UV and NIR beams. The maximum light intensity is obtained at 250 nm, due to the mirror properties. The transmitted light was detected by a photomultiplier tube (Hamamatsu, R928) through a band-pass filter (Sigma Koki, VPF-25C-10-λ, λ = 228, 253 nm, FWHM = 10 nm) or a monochromator (Ritsu, MC-25). The problem in the UV detection is broad overlap of the cross section between HO_2 and RO_2, which is $CH_3OCH_2O_2$ in this case. The cross sections of these species[46] are shown in Figure 3. The $CH_3OCH_2O_2$ was detected at 250 nm considering the UV light intensity and lower interference from HO_2. As the HO_2 component is still included at this wavelength, it was corrected using the FM HO_2 signal. The cross section of $CH_3OCH_2O_2$ at 250 nm is estimated in this setup to be 3.57×10^{-18} cm^2 $molecule^{-1}$, which is 1.2 times higher than in ref 46. The cross section of CH_3OCH_2 is also shown in Figure 3.[47] It was detected at 228 nm, considering the UV light intensity, and the cross section. In the rate constant measurements of CH_3OCH_2 thermal decomposition conducted without O_2, HO_2 interference is not a problem. The cross section of CH_3OCH_2 at 228 nm is 4.76×10^{-18} cm^2 $molecule^{-1}$.[48] Both cross sections are assumed to be independent of temperature in

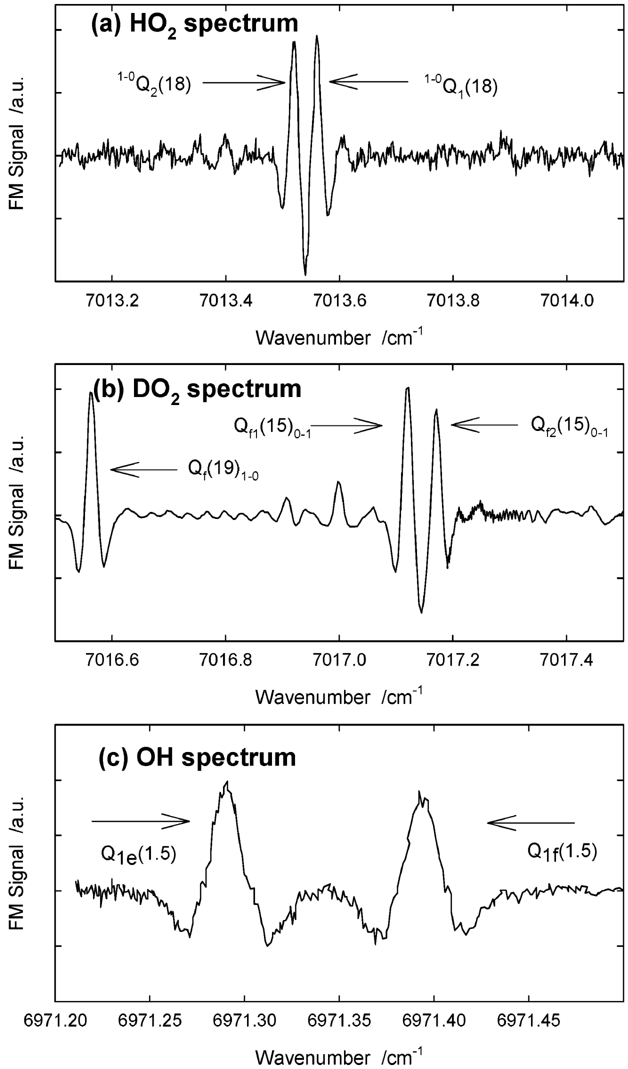

Figure 2. Frequency modulation spectra of (a) HO$_2$, (b) DO$_2$ at the first electronic transition, and (c) OH at the O−H vibrational overtone detected at 298 K. The spectra show a unique shape coming from the second-order frequency modulation spectroscopy. Those species were formed in photolysis of Cl$_2$, O$_2$, and CH$_3$OH (CD$_3$OD) mixtures for HO$_2$ (DO$_2$) and Cl$_2$, O$_2$, CH$_3$OH, and NO mixtures for OH. The initial condition is [Cl$_2$] = 1 × 10^{15}, [O$_2$] = 6 × 10^{16}, [CH$_3$OH = CD$_3$OD] = 1 × 10^{15}, [M] = 1.1 × 10^{18} molecules cm^{-3}, and [NO] = 1 × 10^{15} molecules cm^{-3}.

this study. The peak absorbance was approximately 0.4% under typical experimental conditions.

The length of the UV-probe and photolysis overlap regions was estimated by comparing the HO$_2$ profiles detected by UV and NIR. HO$_2$ was detected at 228 nm, where the recommended value of cross section is 2.8 × 10^{-18} cm^2 molecule^{-1}.[46] The experimental condition is [Cl$_2$] = 1 × 10^{15}, [O$_2$] = 6 × 10^{16}, [DME] = [CH$_3$OH] = 1 × 10^{15}, and total gas density = 1.1 × 10^{18}, all in molecules cm^{-3}. Both time profiles are shown in Figure 4. The HO$_2$ profiles show a rapid rise at photolysis, followed by a gradual decrease by the rate of HO$_2$ self-reaction. The half-life time of HO$_2$ detected by UV is approximately 6.5 ms, which is consistent with that of the NIR profile. Since the rate constant of HO$_2$ is given to be 3.0 × 10^{-12} cm^3 molecule^{-1} s^{-1},[49] the initial HO$_2$ concentration is estimated to be approximately 5.1 × 10^{13} molecules cm^{-3}. This value is in good agreement with initial chlorine atom concentration derived from the photolysis laser fluence at this experimental condition. As the initial absorbance (A = - ln (I/I_0)) is approximately 0.6 ± 0.06%, the absorption length was estimated to be 40 ± 4 cm on the basis of the Beer−Lambert law. This length is applied to the following kinetic analysis.

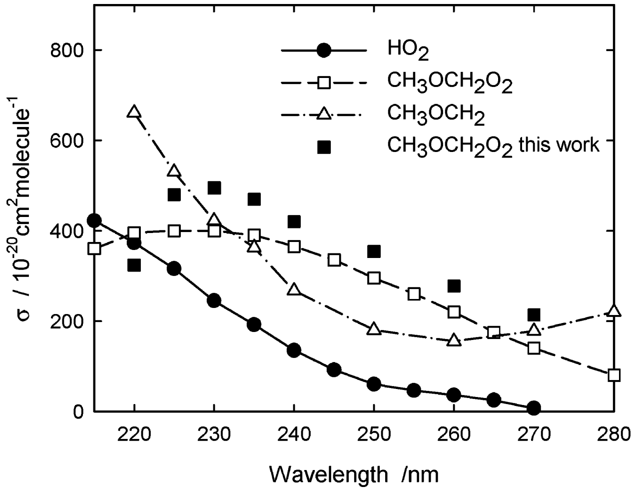

Figure 3. Cross section of HO$_2$, CH$_3$OCH$_2$O$_2$,[46] and CH$_3$OCH$_2$.[47] The square symbols show our estimation using the estimated overlap length (40 cm) and the model consideration of initial CH$_3$OCH$_2$O$_2$ yield (86%).

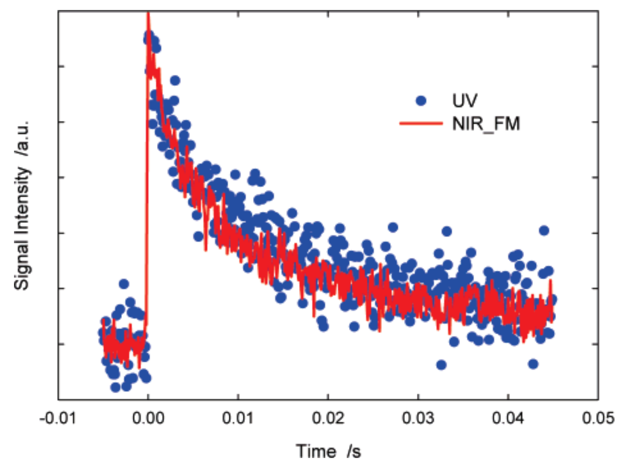

Figure 4. HO$_2$ time profiles detected by UV and NIR techniques under the condition of [Cl$_2$] = 1 × 10^{15}, [O$_2$] = 6 × 10^{16}, [CH$_3$OH] = 1 × 10^{15}, and [M] = 1.1 × 10^{18} molecules cm^{-3}, at 298 K.

Results and Discussion

A. Measurements of Products. To investigate the mechanism of HO$_2$ formation in the reaction of CH$_3$OCH$_2$ + O$_2$, HO$_2$, OH, and CH$_3$OCH$_2$O$_2$ have been detected using above-described techniques. The time profiles of these species at 600 and 298 K are shown in Figure 5. Reference signals of HO$_2$ at both temperatures show a prompt rise under photolysis, followed by a gradual decrease by the rate of HO$_2$ + HO$_2$ self-reaction. In contrast, the HO$_2$ signal from the CH$_3$OCH$_2$ + O$_2$ at 600 K exhibits a slow rise, followed by a gradual decay, similar to the previously investigated cases of ethane, propane, and cyclopentane.[6−9] The HO$_2$ signal from CH$_3$OCH$_3$ at 298 K begins with a fast but weak rise and levels off, which indicates that steady HO$_2$ formation balances with the consumption rate. OH profiles from CH$_3$OCH$_2$ + O$_2$ show rapid rises, similar to the previous cases.[11,13] This is consistent with the HCHO formation having a fast component, as reported by Rosado-Reyes et al.[38] The peak amount of OH, particularly reaching over half that of the reference at 600 K, is considerably larger than those of ethane, propane and neopentane.[11,13] These results

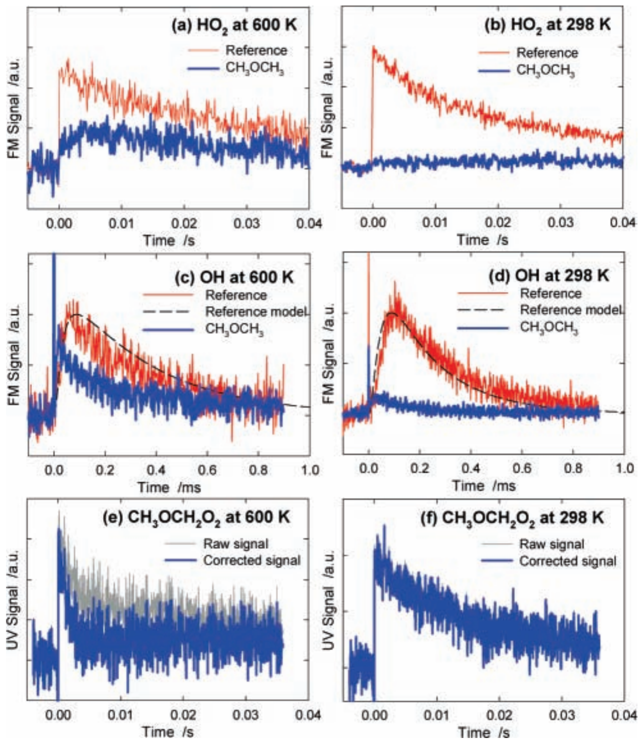

Figure 5. Time profiles of (a, b) HO_2, (c, d) OH, and (e, f) $CH_3OCH_2O_2$ at 600 and 298 K. Thin blue lines are from the photolysis of $Cl_2/O_2/CH_3OCH_3$ mixtures. Thin red lines are from the photoysis of reference mixtures. Gray lines in the $CH_3OCH_2O_2$ time profiles are raw UV signals before correction for HO_2 contribution. The initial condition is $[Cl_2] = 2 \times 10^{14}$, $[O_2] = 1.2 \times 10^{16}$, $[CH_3OH] = 1 \times 10^{15}$ molecules cm^{-3} for HO_2, $[Cl_2] = 1 \times 10^{15}$, $[O_2] = 6 \times 10^{16}$, $[CH_3OH] = 1 \times 10^{15}$ molecules cm^{-3} for OH and $CH_3OCH_2O_2$, all in a total gas density of 1.1×10^{18} molecules cm^{-3}.

suggested that the OH formation pathway is more favorable than in C_2 and C_3 alkyl radicals. The $CH_3OCH_2O_2$ profiles at both temperatures have a rapid rise and a gradual decay, but with different decay time constants. It seems that the relatively fast decay at 600 K corresponds to the HO_2 formation and the 298 K decay to the $CH_3OCH_2O_2$ self-reaction.

In order to obtain the overall HO_2 yield, the procedure of profile correction developed by Taatjes et al. was performed.[6] Originally this procedure can correct the raw profile for the decay caused by HO_2 self-reaction and $HO_2 + RO_2$ reaction. However, in this study only the HO_2 self-reaction was considered because of the lack of direct measurement for the rate constant of $HO_2 + CH_3OCH_2O_2$. The upper limit of the yield, including the correction with the $HO_2-CH_3OCH_2O_2$ reaction, was estimated to be approximately 70% at 600 K and to be approximately 20% at 298 K, respectively, using the $CH_3OCH_2O_2$ profile obtained in the UV measurement and assuming a rate constant of $5.65 \times 10^{-13} \times \exp(5.3\ \text{kJ/mol}/RT)$ cm^3 $molecule^{-1}$ s^{-1},[17] which is the largest estimate for this reaction. Even in this case, the yield is below unity, which is different from that of C_2 and C_3 alkanes.

The yield of OH was also obtained using another procedure simulating the rise and decay profiles due to fast OH consumption reactions.[11,13] The dashed line in Figure 5, parts c and d, was the result of using the model shown in Table 1, which is in good agreement with the reference signals.

The UV signal at 250 nm was corrected for the pure $CH_3OCH_2O_2$ profile by removing the HO_2 component using the FMS signal of HO_2. The conversion factor was determined by the comparison, as demonstrated in Figure 4. The observed absorbance, the effective absorption length (40 cm), HO_2 cross section at 250 nm (6.6×10^{-19} cm^2 $molecule^{-1}$)[46] and the concentration estimate from the decay rate due to HO_2 self-reaction are consistent. At 600 K, the maximum absorbance of HO_2 was approximately 0.5%. The raw and corrected signals are shown in Figure 5, parts e and f.

The temperature dependence of overall HO_2 yield, OH peak yield, and $CH_3OCH_2O_2$ peak yield, which are the ratio to initial Cl concentration determined by laser influence and decay of reference HO_2 signals, are shown in Figure 6. The HO_2 yield gradually increases until 500 K and rapidly increases toward 600 K. The yield of HO_2 below 500 K is a few percent higher than that of ethane and propane. The OH yield increases gradually with increasing temperature in this temperature range. The peak yield ranged between 10% and 40%, 1 order of magnitude larger than observed for ethane and propane[13] and also larger than that of neopentane.[11] The $CH_3OCH_2O_2$ peak yield gradually decreases until 500 K and sharply decreases toward 600 K. This suggests that the mechanism of $CH_3OCH_2O_2$ consumption changes at 500 K. While the slow decay corresponds to the rate of $CH_3OCH_2O_2$ self-reaction, the positive temperature dependence over 500 K is a property of thermal decomposition.

The pressure dependence of HO_2 prompt yield, and OH and $CH_3OCH_2O_2$ peak yields are also shown in Figure 6, parts b, d, and f. The HO_2 and OH show weak negative pressure dependence and $CH_3OCH_2O_2$ shows a weak positive dependence. A similar pressure dependence of HO_2 yield was observed in the cases of ethane and propane.[7,8]

B. HO_2 Formation at 600 K. The time profiles of HO_2, OH, and $CH_3OCH_2O_2$ scaled relative to the initial chlorine atom concentration are shown in Figure 7. The corrected reference signal leveling off at unity indicates that the decay is dominated by the HO_2 self-reaction. The correction for the DME signal is not significant, owing to the low concentration. The peak yield of $CH_3OCH_2O_2$ is approximately 40% and the part following decay is noticeably fast. This indicates that the $CH_3OCH_2O_2$ formation rate is comparable to that of consumption, which may be either $CH_3OCH_2O_2$ decomposition or CH_3OCH_2 decomposition.

The HO_2 formation pathway depicted from the model of Curran et al.[19] consists of reactions 9−11 and following reactions:

$$HCHO + OH \rightarrow HCO + H_2O \tag{18}$$

$$HCO + O_2 \rightarrow HO_2 + CO \tag{19}$$

OH is consumed by HCHO and CH_3OCH_3 competitively

$$CH_3OCH_3 + OH \rightarrow CH_3OCH_2 + H_2O \tag{20}$$

The CH_3OCH_2 thermal decomposition reaction competes with the $CH_3OCH_2 + O_2$ reaction over 550 K.[39]

$$CH_3OCH_2\ (+M) \rightarrow HCHO + CH_3\ (+M) \tag{21}$$

This mechanism with the original set of rate constants does not predict the experimental results such as the OH rapid rise and the amount of HO_2 at 600 K, as superimposed in Figure 7. One important point is that the Curran et al. model has been established to represent higher pressure reactors like shock tubes and jet stirred reactors.

Accordingly, we have constructed a modified model for this reduced-pressure photolytically initiated system, as shown in Table 2. The model of pulsed-photolytic Cl-initiated reaction

TABLE 1: Reaction Rate Constants Used to Model the OH Reference Signal Initiated by Pulsed Photolysis in the Mixture of $Cl_2/O_2/CH_3OH/NO$[a]

reaction	*A*	*n*	*E*	ref
$CH_3OH + Cl \rightarrow CH_2OH + HCl$	3.31×10^{13}	0	0	48
$CH_2OH + O_2 \rightarrow HO_2 + CH_2O$	4.56×10^{-6}	5.94	−4539	49
$HO_2 + NO \rightarrow OH + NO_2$	2.11×10^{12}	0	−497	50
$HO_2 + HO_2 \rightarrow H_2O_2 + O_2$	1.3×10^{11}	0	−1629	51
$HO_2 + HO_2 \rightarrow H_2O_2 + O_2$	4.2×10^{14}	0	11 980	52
$OH + HO_2 \rightarrow H_2O + O_2$	2.89×10^{13}	0	−497	53
$OH + CH_3OH \rightarrow CH_2OH + H_2O$	1.44×10^{6}	2	−841	54
$NO + OH(+M) \rightarrow HNO_2(+M)$	2.0×10^{13}	0	0	55
low	2.33×10^{23}	−2.4	0	
$OH + OH \rightarrow O + H_2O$	1.75×10^{4}	2.6	−1878	56
$OH + OH(+M) \rightarrow H_2O_2(+M)$	1.24×10^{14}	−0.37	0	57
low	3.04×10^{30}	−4.63	2049	
Troe	0.47	100	2000	1×10^{15}
$H_2/2/H_2O/12/CO/1.9/$				
$OH + CH_2O \rightarrow HCO + H_2O$	3.44×10^{9}	1.18	−447	58
$OH + HCO \rightarrow CO + H_2O$	3.01×10^{13}	0	0	58
$OH + NO_2(+M) \rightarrow HNO_3(+M)$	2.4×10^{13}	0	0	59
low	6.42×10^{32}	−5.49	2351	
Troe	0.525	1.0×10^{-15}	1.0×10^{-15}	1.0×10^{15}
$H_2O/5.0/$				
$OH + HNO_2 \rightarrow H_2O + NO_2$	1.26×10^{10}	1	135	59
$HCO + O_2 \rightarrow HO_2 + CO$	7.59×10^{12}	0	405	60
$NO + CH_2OH \rightarrow CH_2OH(NO)$	1.51×10^{13}	0	0	61

[a] The rate constants are written in the form of $A \times T^n \times \exp(-E/RT)$. The unit of *A* is $cm^3\ mol^{-1}\ s^{-1}$ for bimolecular reactions and $cm^6\ mol^{-2}\ s^{-1}$ for termolecular reactions. The unit of E is cal/mol."low" shows the rate constant of the low-pressure limit. "Troe" shows the parameter of the Troe formula, $F_{cent} = (1 - \alpha)\exp(-T/T^{***}) + \alpha\exp(-T/T^{*}) + \exp(-T^{**}/T)$ from the left, in order, where *T* is the temperature.

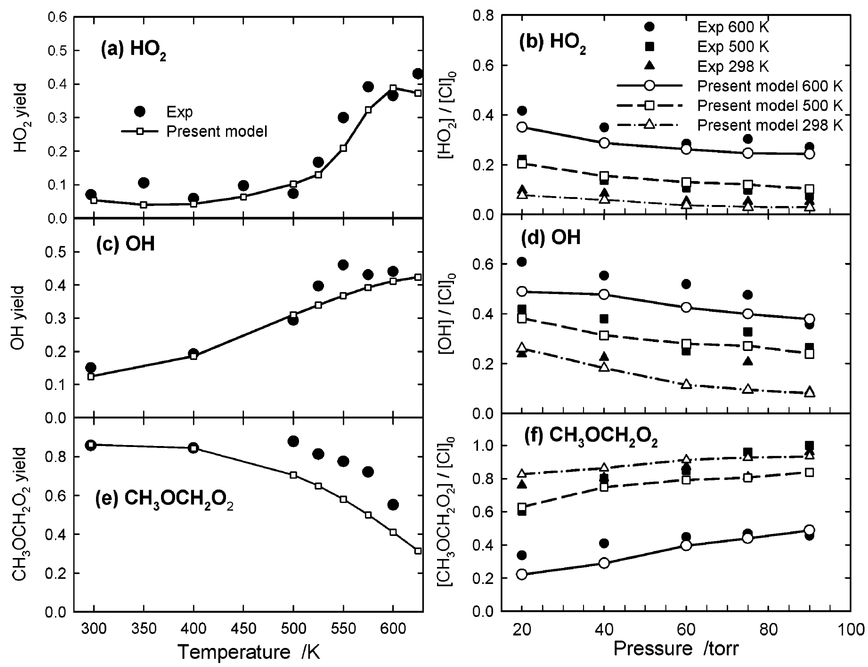

Figure 6. Yields of (a, b) overall HO_2, (c, d) peak OH, and (e, f) peak $CH_3OCH_2O_2$ as a function of temperature and pressure. Solid symbols are experimental results and lines with open symbols are calculated results using our model shown in Table 2.

of neopentyl + O_2[11] was also referenced. An important modification is pressure dependence of unimolecular reactions 9−11 and 21, for which originally the high-pressure limit was given. The pressure dependent rate constant of the CH_3OCH_2 decomposition reaction 21 has been measured in this study, as described later. (The rate constant of this reaction at 600 K and 68 Torr is $1.06 \times 10^3\ s^{-1}$, which is 8 times lower than in the Curran et al. model.) The pressure dependent rate constants of reactions 9−11 were first taken from the Yamada et al. evaluation, which were calculated with the CBS-q level of theory and the QRRK method,[35] and considered modification. These rate constants are expressed in Troe form as shown in Table 2. After the adjustment to fit the experimental profiles, the rate constant of the $CH_2OCH_2O_2H$ decomposition reaction is 10 times higher than the original one.

To represent the prompt OH formation and fairly rapid HO_2 formation, the direct formation from R + O_2 reaction and one of the HO_2 formation reactions suggested in the neopentyl + O_2 reaction model are considered.

$$CH_3OCH_2 + O_2 \rightarrow OH + 2HCHO \qquad (22)$$

$$OH + CH_3OCH_2O_2 \rightarrow HO_2 + CH_3OCH_2O \qquad (23)$$

Since there are no measurements of the rate constant of reaction (23), we assumed $k_{23} = 4.0 \times 10^{-11}\ cm^3\ molecule^{-1}\ s^{-1}$ after

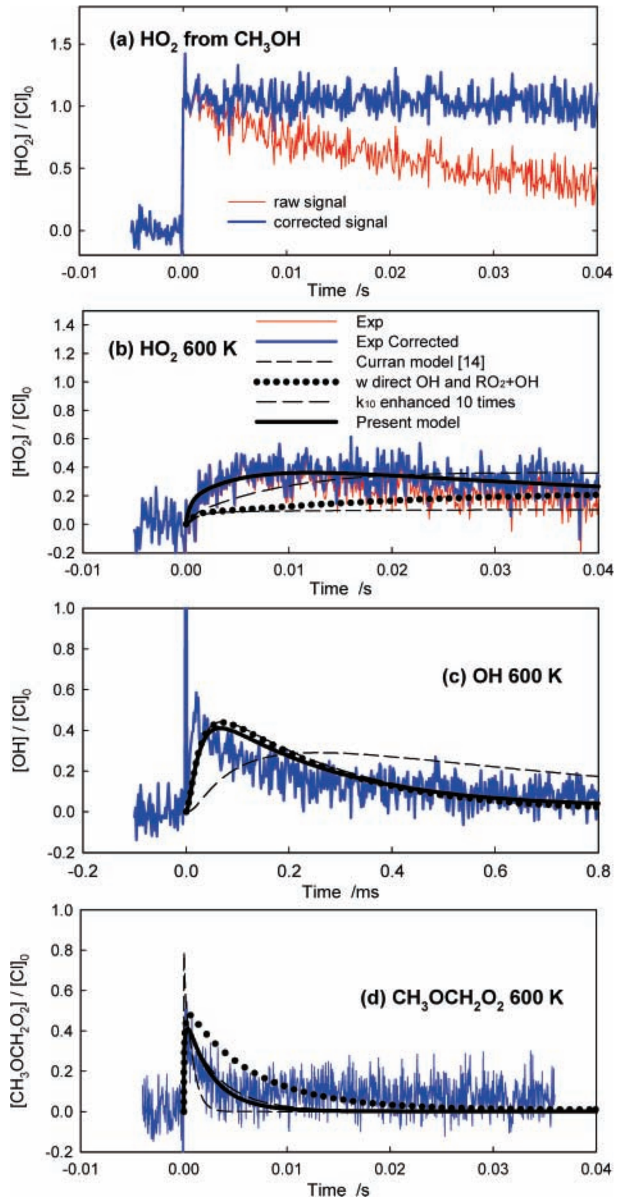

Figure 7. Scaled time profiles relative to initial chlorine atom concentration at 600 K. (a) HO_2 from reference mixture ($Cl_2/O_2/CH_3OH$), (b) HO_2, (c) OH, and (d) $CH_3OCH_2O_2$ from the CH_3OCH_3 mixture ($Cl_2/O_2/CH_3OCH_3$). Blue and gray lines are calculated profiles from each stage of modeling described in the text.

the case of neopentane,[15] which originally is the rate of CF_3O_2 + OH.[65] The rate constant of reaction 22 is set as $k_{22} = 4.0 \times 10^{-13}$ cm^3 molecule^{-1} s^{-1} to represent the OH formation as shown in Figure 7c. Even when reactions 22 and 23 were considered, the amount of HO_2 formation was only approximately 40% that of the experiment. In addition, the $CH_3OCH_2O_2$ decay was still considerably slower than experimentally observed, although reaction 23 greatly accelerated the decay.

In this state of the model, the dominant HO_2 formation pathway is via HCHO + OH and HCO + O_2 reactions. In order to achieve the amount of HO_2 within the framework, the amount of HCHO and OH needs to be increased. This was done by further enhancing the $CH_2OCH_2O_2H$ decomposition rate 10 times; however, it overestimated the $CH_3OCH_2O_2$ decay rate and the HO_2 rise rate is still underestimated.

Accordingly, the direct formation of HCO was assumed:

$$CH_3OCH_2 + O_2 \rightarrow HCO + H_2O + HCHO \qquad (24)$$

The rate constant of reaction 24 was determined to fit the HO_2 formation, keeping reactions 9 and 22 intact. When $k_{24} = 5.8 \times 10^{-14}$ cm^3 molecule^{-1} s^{-1} was assumed, the HO_2, OH, and $CH_3OCH_2O_2$ profiles at 600 K were successfully modeled. The diffusion rate, which is specific to this experiment and estimated as 12 s^{-1}, was also considered.[40] Note that reactions 10 and 11 simply act as a series reaction under these experimental conditions so that only the product of these rate constants is essential. As understood later, the absolute rate constant of reaction 9 is unimportant, provided that the excess oxygen ensures the completion of reaction 9, while the CH_3OCH_2 decomposition does not contribute.

The remaining concern is the OH profile on which the current calculation does not perfectly model the experiment, particularly at the rise rate. For this part not only the above-mentioned OH formation/consumption reactions, but also the preceding reactions such as $CH_3OCH_2O_2$ formation are responsible. Because of the insufficient time resolution in HO_2 and $CH_3OCH_2O_2$ detection under the current experimental conditions, we settle with this state of the model.

Ab Initio Calculation of Potential Energy Surface. Previous theoretical studies[35-37] on the CH_3OCH_2 + O_2 reactions suggested that the dominant products are 2 HCHO + OH via the fission of CH_2OCH_2OOH and the potential barrier for the channel of HO_2 + CH_2OCH_2 formation is so high that direct formation of HO_2 from CH_3OCH_2 + O_2 was not considered in the DME oxidation model. These computational results are mostly consistent with the experimental results, in which HCHO was formed primarily,[37] but seem insufficient to account for the present observation of rapid HO_2 formation. We therefore investigated the potential energy surface of the CH_3OCH_2 + O_2 reactions by using ab initio molecular orbital calculations, particularly for undiscovered channels.

First, we employed density functional methods to survey the potential energy surface of the CH_3OCH_2 + O_2 system. Most minima and transition states (TS) were optimized using the B3PW91 hybrid density functional method and cc-pVTZ basis set. The G2M(CC1) calculations[69] were performed at the B3PW91/cc-pVTZ optimized geometry in order to determine more accurate energies. These calculations were conducted with Gaussian 98 and 03 codes.[70,71]

MRMP//CASSCF calculations were further executed for the transition states of key reaction channels by using GAMESS.[72] Geometry of CH_2OCH_2OOH (shortly QOOH) and transition states in consecutive reaction steps were finally optimized at the CASSCF(17,14)/VTZ level. The active space of the CASSCF(17,14) calculations consist of the highest singly occupied molecular orbital, the bonding and antibonding orbital of C−O, O−O and O−H bonds and a lone pair orbital of the each oxygen atom. Vibrational analysis was conducted at the CASSCF(17,14)/VTZ level. The MRMP energy calculations were performed at the CASSCF(17,14)/VTZ optimized geometry. The MRMP energy of the transition states was compared with that of CH_2OCH_2OOH, and was converted to relative one to CH_3OCH_2 + O_2, where the G2M(UCC1) energy of −111 kJ mol^{-1} was employed as the relative energy of CH_2OCH_2-OOH to CH_3OCH_2 + O_2. Results of the PES calculations are illustrated in Figure 8. In the same figure, wells and the transition states with asterisk on the shoulder represent that the potential energy was obtained by the MRMP/CASSCF methods.

Transition structures for three-body fission (TS3: QOOH → 2HCHO + OH), two-body fission (TS4: QOOH → HCHO + CH_2OOH), the elimination of OH (TS5: QOOH → OH + HCHO dimer), HO_2 (TS6: QOOH → HO_2 + C_2H_4O), and H

TABLE 2: Kinetic Model for Cl Initiated Oxidation of CH_3OCH_3[f]

reaction	*A*	*n*	*E*	ref
$Cl + CH_3OCH_3 \rightarrow CH_3OCH_2 + HCl$	1.06×10^{14}	0	0	62
$CH_3OCH_2 + Cl_2 \rightarrow CH_3OCH_2Cl + Cl$	1.08×10^{13}	0	720	34
$CH_3OCH_2\ (+M) \rightarrow CH_3 + CH_2O + (M)$	1.60×10^{13}	0	25 500	63[a]
low	2.8×10^{16}	0	18100	
Troe	0.5	350	450	
$CH_3OCH_2 + O_2 + (M) \rightarrow CH_3OCH_2O_2\ (+M)$	5.82×10^{12}	0	0	35
low	1.04×10^{16}	0	−6436	
Troe	0.312	246	5.9×10^{-4}	
$CH_3OCH_2O_2\ (+M) \rightarrow CH_2OCH_2O_2H\ (+M)$	6.54×10^{10}	0	18 220	35
low	2.33×10^{15}	0	11430	
Troe	0.25	2088	1.04×10^{-4}	
$CH_2OCH_2O_2H(+M) \rightarrow OH + 2HCHO\ (+M)$	1.16×10^{14}	0	20 560	35[b]
low	3.2×10^{19}	0	19400	
Troe	−2.69	163	1.09×10^{-5}	
$CH_3OCH_2 + O_2 \rightarrow OH + 2HCHO$	9.33×10^{10}	0	−1127	this work
$CH_3OCH_2 + O_2 \rightarrow HCO + H_2O + CH_2O$	6.67×10^{10}	0	773	this work
$CH_2OCH_2O_2H + O_2 \rightarrow O_2CH_2OCH_2O_2H$	9.0×10^{11}	0	0	19
$CH_2O + OH \rightarrow HCO + H_2O$	3.44×10^{9}	1.18	−447	58
$HCO + O_2 \rightarrow HO_2 + CO$	7.59×10^{12}	0	405	60
$CH_3OCH_3 + OH \rightarrow CH_3OCH_2 + H_2O$	6.03×10^{12}	0	735	48
$CH_3 + Cl_2 \rightarrow CH_3Cl + Cl$	2.88×10^{12}	0	477	60
$CH_3 + O_2\ (+M) \rightarrow CH_3O_2\ (+M)$	7.83×10^{8}	1.2	0	64
$HO_2 + HO_2 \rightarrow H_2O_2 + O_2$	1.3×10^{11}	0	−1629	51
$HO_2 + HO_2 \rightarrow H_2O_2 + O_2$	4.2×10^{14}	0	11 980	52
$CH_3OCH_2O_2 + CH_3OCH_2O_2 \rightarrow CH_3OCHO + CH_3OCH_2OH + O$	5.42×10^{10}	0	−1390	38[c]
$CH_3OCH_2O_2 + CH_3OCH_2O_2 \rightarrow 2CH_3OCH_2O + O_2$	1.261×10^{11}	0	−1390	38[c]
$CH_3O_2 + CH_3O_2 \rightarrow 2CH_3O + O_2$	5.48×10^{10}	0	−834	53
$CH_3O + O_2 \rightarrow CH_2O + HO_2$	2.17×10^{10}	0	1747	53
$OH + CH_3OCH_2O_2 \rightarrow HO_2 + CH_3OCH_2O$	2.41×10^{13}	0	0	65[d]
$OH + HO_2 \rightarrow H_2O + O_2$	2.89×10^{13}	0	−497	53
$Cl + CH_2O \rightarrow HCl + HCO$	4.94×10^{13}	0	68	48
$CH_3 + CH_2O \rightarrow CH_4 + HCO$	7.77×10^{-8}	6.1	1976	53
$OH + OH \rightarrow H_2O + O$	1.5×10^{9}	1.14	99	64
$CH_3OCH_2O_2 + HO_2 \rightarrow CH_3OCH_2O_2H + O_2$	2.29×10^{11}	0	−1790	66[e]
$CH_3OCH_2O \rightarrow CH_3OCHO + H$	3.0×10^{5}	0	0	38
$H + O_2\ (+M) \rightarrow HO_2\ (+M)$	1.48×10^{12}	0.6	0	67
low	3.5×10^{16}	−0.41	−1120	
Troe	0.5	1×10^{-30}	1×10^{30}	
$H_2/2.5/H_2O/12/CO/1.9/CO_2/3.8/$	3.61×10^{10}	0	1092	38
$CH_3OCH_2O + O_2 \rightarrow CH_3OCHO + HO_2$				
$OH + OH + M \rightarrow H_2O_2 + M$	2.38×10^{19}	−0.8	0	48
$OH + HCO \rightarrow CO + H_2O$	3.01×10^{13}	0	0	58
$H + Cl_2 \rightarrow Cl + HCl$	8.59×10^{13}	0	0	68
HO_2 diffusion	12			this work

[a] The rate constant is obtained for the pressure range 20−90 Torr in this study. The data of ref 63 is applied to high and low-pressure limits. [b] The rate constant is enhanced 10 times from the original of ref 40. [c] Jenkin et al.'s data[38] is applied to the branching ratio of these reactions, which are assumed to have no temperature dependence. [d] The temperature-independent rate constant of the CF_3O_2 + OH reaction is assumed to be this reaction rate constant. [e] The rate constant of $C_2H_5O_2 + HO_2$ is adopted. [f] The unit of *A* is s^{-1} for first-order reactions, $cm^3\ mol^{-1}\ s^{-1}$ for bimolecular reactions, and $cm^6\ mol^{-2}\ s^{-1}$ for termolecular reactions. The unit of E is cal/mol. "low" and "Troe" are the same as in Table 1.

atom (TS7: QOOH → H + 1,2,4-trioxolane) were successfully obtained at the CASSCF(17,14)/VTZ level of theory. The transition structure of H atom transfer (TS1: RO_2 → QOOH) was also obtained at the same level. However, the CASSCF-(17,14)/VTZ calculations failed to attain the geometry of the transition state of OH transfer (TS2: QOOH → HOQO), owing to misconvergence occurring for neighboring geometries. This seems to be attributed to the fact that the active space is not sufficient for OH transfer. The transition structure of TS2 was obtained with CASSCF(19, 14)/VDZ, for which residual two lone pair orbitals of two oxygen atoms in −OOH were added to and the bonding and antibonding orbitals of the CH_2O−COOH bond were excluded from the active space of the CASSCF(17,14). The reason for the latter elimination is the lack of our computational resources.

The addition of O_2 to CH_3OCH_2 proceeds without an intervening potential energy barrier to form $CH_3OCH_2O_2$. Except for dissociation back to the reactants, the reaction of $CH_3OCH_2O_2$ occurs via intramolecular migration of the H atom to form CH_2OCH_2OOH. The potential barriers of TS2, TS3, TS4, and TS5 are all lower than the entrance energy of $CH_3OCH_2 + O_2$. Therefore, any channel via these transition states has the possibility of being an actual reaction pathway. Considering that the results were due to the MRMP//CASSCF calculations with a limited active space and uneven basis sets, especially for TS2, we hesitate to discuss the difference in barrier heights among them. It is noted, however, that TS2 is a tight transition state, whereas TS3 and TS4 are loose ones, so the dissociation of CH_2OCH_2OOH via the latter transition states are favorable in entropy. Apart from the free energy of each transition state, the channel via TS2 has the advantage of becoming the dominant course of the $CH_3OCH_2 + O_2$ reactions at lower temperature because barrier penetration by tunneling at TS2 is much greater than that in other transition states. The barrier height of TS6 and TS7 are entirely over the entrance energy, so the product channels of $HO_2 + C_2H_4O$ via TS6 and $H + C_2H_4O_3$ via TS7 are unlikely as actual reaction courses.

$HOCH_2OCH_2O$ via TS2 on the potential energy surface connects to 2HCHO + OH (via TS8), HCO + HCHO + H_2O (via TS9), as products of fission or migration. All the above

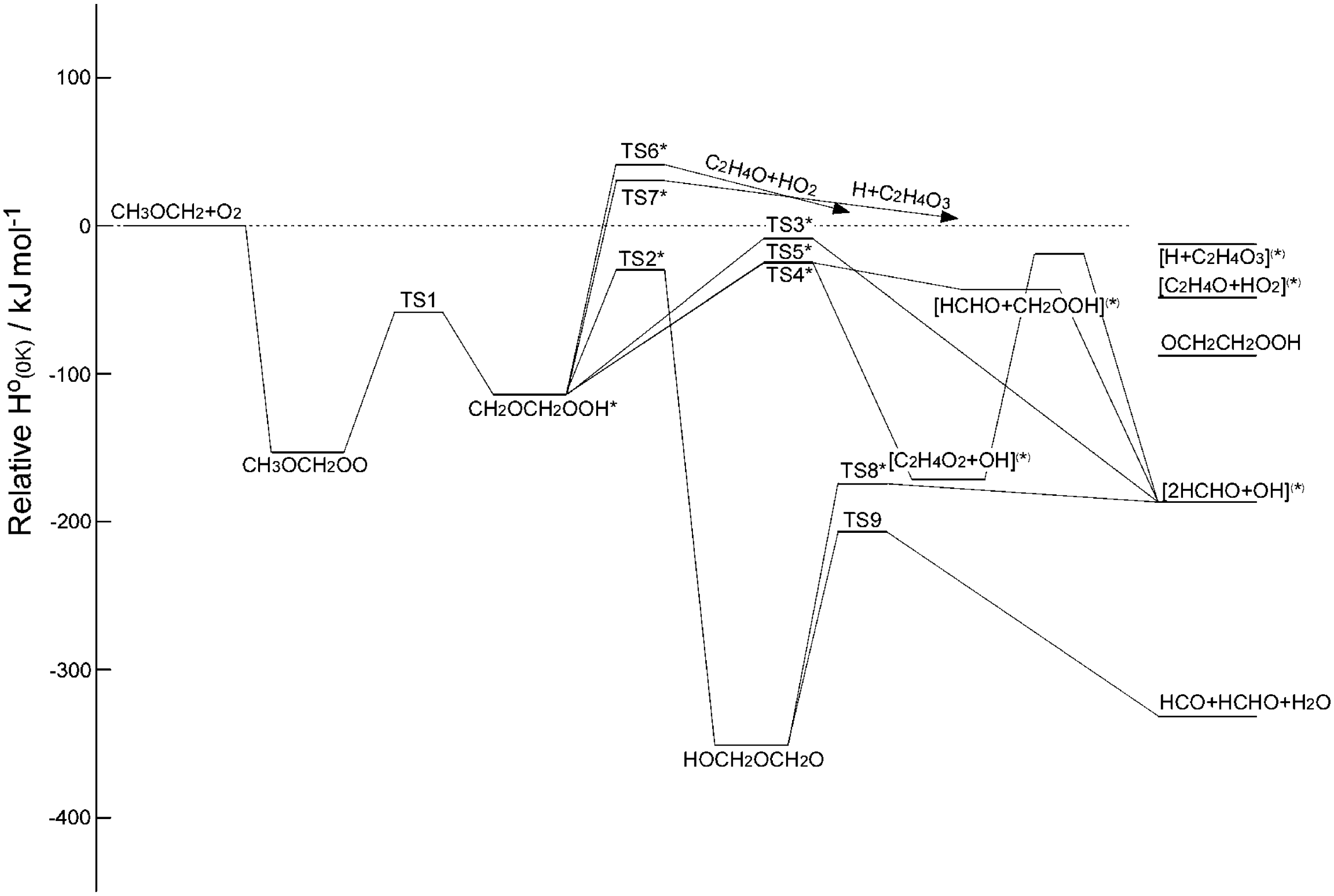

Figure 8. Potential energy diagram of the $CH_3OCH_2 + O_2$ reaction. Wells and the transition states with asterisk on the shoulder represent that the potential energy was obtained by the MRMP/CASSCF methods.

product channels are energetically promising because their respective intervening barriers are lower than that of TS2. TS8 is a looser transition state than TS9, which indicates that the decomposition of CH_2OCH_2OOH* via TS2 partly contributes to form 2HCHO + OH. End-products specific to the reaction channels via TS2 are CO, HO_2. Consequently, the reaction course via TS2, which was not considered in the previous theoretical studies, seems to contribute to a certain extent to the formation of HO_2 observed in the experiments.

The Rate Constant of the CH_3OCH_2 Thermal Decomposition Reaction. In this study, the rate constant of the CH_3OCH_2 thermal decomposition reaction has been measured using the UV absorption technique. Loucks et al. reported only high and low-pressure limits for this reaction.[63] The measurements were conducted in the temperature range 600−700 K and the pressure range 20−90 Torr. The experimental condition was $[Cl_2] = 5 \times 10^{14}$, $[DME] = 1 \times 10^{15}$ molecules cm^{-3} with He buffer. The reaction is initiated by pulsed photolysis in a mixture of Cl_2/CH_3OCH_3. The CH_3OCH_2 were measured at 228 nm ($\sigma = 4.76 \times 10^{-18}$ cm^2 molecule^{-1}) with a peak absorbance of approximately 0.4%.

A typical time profile of CH_3OCH_2 at 650 K and 60 Torr is shown in Figure 9. After the initial few tens of microseconds that were blind due to the photolysis shot noise, the CH_3OCH_2 decays in a single-exponential manner. Under this condition, CH_3OCH_2 is consumed by thermal decomposition and self-reaction, i.e.;

$$CH_3OCH_2\ (+M) \rightarrow CH_3 + HCHO\ (+M) \quad (25)$$

$$CH_3OCH_2 + CH_3OCH_2 \rightarrow CH_3OCH_2CH_2OCH_3 \quad (26)$$

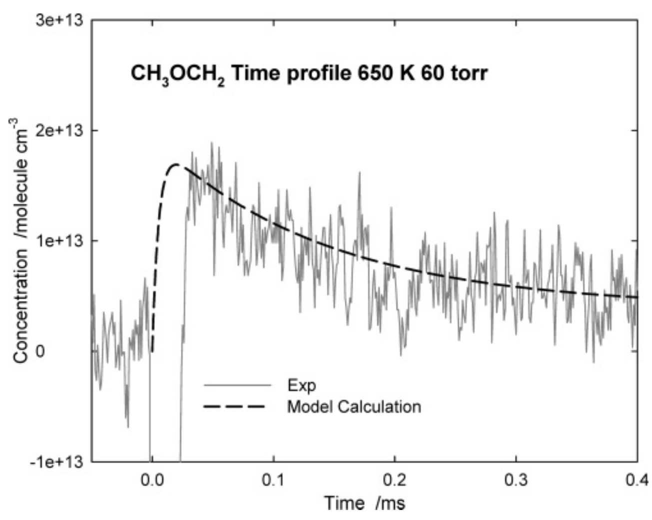

Figure 9. CH_3OCH_2 time profile at 650 K, 60 Torr showing the decay due to the thermal decomposition reaction. The initial concentration is $[Cl_2] = 5 \times 10^{14}$, $[DME] = 1 \times 10^{15}$ molecules cm^{-3} with He buffer. The dashed line is the model profile considering the $CH_3 + Cl_2$ reaction. Note that the initial 20 μs is the region interfered with by the photolysis shot noise.

and CH_3 from reaction 25 also reacts with Cl_2 forming Cl,

$$CH_3 + Cl_2 \rightarrow Cl + CH_3Cl \quad (27)$$

where the rate constant is known as $k_{27} = 4.78 \times 10^{-12} \times \exp(-477\ (\text{cal/mol})/RT)$ cm^3 molecule^{-1} s^{-1}.[60] This Cl reacts with CH_3OCH_3 to reproduce CH_3OCH_2. By fitting the model profile with the above reactions, the rate constant k_{25} was determined.

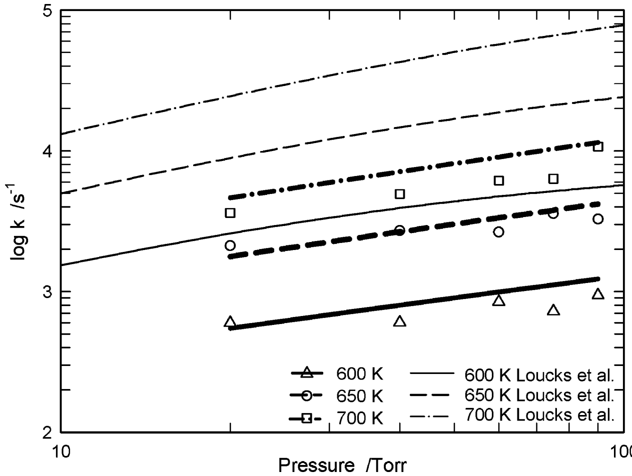

Figure 10. Rate constant of CH_3OCH_2 decomposition reaction as a function of pressure. Symbols are measurement results, bold lines are fitting using the Troe form expression, and thin lines are the Lindemann interpolation of high and low-pressure limits from Loucks et al.[63]

The predicted profile is also shown in Figure 9. The obtained rate constant is shown as a function of pressure in Figure 10. The present rate constant is lower than that of the Lindemann interpolation from Loucks et al. by a factor of 0.2. Three parameters of Troe form are determined as shown in Table. 2. The high and low-pressure limits are assumed as those of Locks et al. However, although the fitting curves look reasonable, the bath gas (DME) is different from ours. Accordingly, this expression should be considered as a practical interpolation valid within the present experimental range.

C. HO_2 formation at 298 K. Time profiles of detected species at 298 K scaled by the same procedure as in 600 K are shown in Figure 11. The overall yield of HO_2 throughout the lower temperature region is approximately 10% as shown in Figure 6, which is larger than in the C_2 and C_3 alkanes.[11,12] The time profile also behaves differently, which keeps a steady nonzero level after the initial rise, unlike the decay profiles of ethyl and propyl.[11,12] OH is also produced at approximately 10%. Once $CH_3OCH_2O_2$ is thermally stabilized, its isomerization and decomposition reactions are unlikely at this temperature; hence, HO_2 should be produced by other pathways. The room-temperature oxidation mechanism of DME has been suggested by Jenkin et al. in 1993[73] and Rosado-Reyes et al. in 2005.[38] According to Jenkin et al., HO_2 is formed as

$$CH_3OCH_2O_2 + CH_3OCH_2O_2 \rightarrow 2CH_3OCH_2O + O_2 \quad (28\text{-a})$$

$$CH_3OCH_2O_2 + CH_3OCH_2O_2 \rightarrow CH_3OCHO + CH_3OCH_2OH + O_2 \quad (28\text{-b})$$

$$CH_3OCH_2O\ (+M) \rightarrow CH_3OCHO + H\ (+M) \quad (29)$$

$$CH_3OCH_2O + O_2 \rightarrow HO_2 + CH_3OCHO \quad (30)$$

$$H + O_2\ (+M) \rightarrow HO_2\ (+M) \quad (31)$$

$CH_3OCH_2O_2$ decreases by its self-reaction in this temperature range. Jenkin et al. obtained the rate constant of the self-reaction at 298 K as $k_{28} = 2.1 \times 10^{-12}$ cm^3 molecule^{-1} s^{-1} and the branching ratio as $k_{28a}/k_{28} = 0.7$. Rosado-Reyes et al. also obtained the temperature dependence of this reaction as $k_{28} = 3.0 \times 10^{-13} \exp(700/T)$ cm^3 molecule^{-1} s^{-1} between 295 and 650 K. The rate constants of reactions 29 and 30 are also reported. In that model, the direct formation of OH is considered. The time profiles of HO_2, OH and $CH_3OCH_2O_2$ calculated using the Rosado-Reyes et al. model are shown in Figure 11. The OH profile was well predicted, whereas the HO_2 and $CH_3OCH_2O_2$ are not.

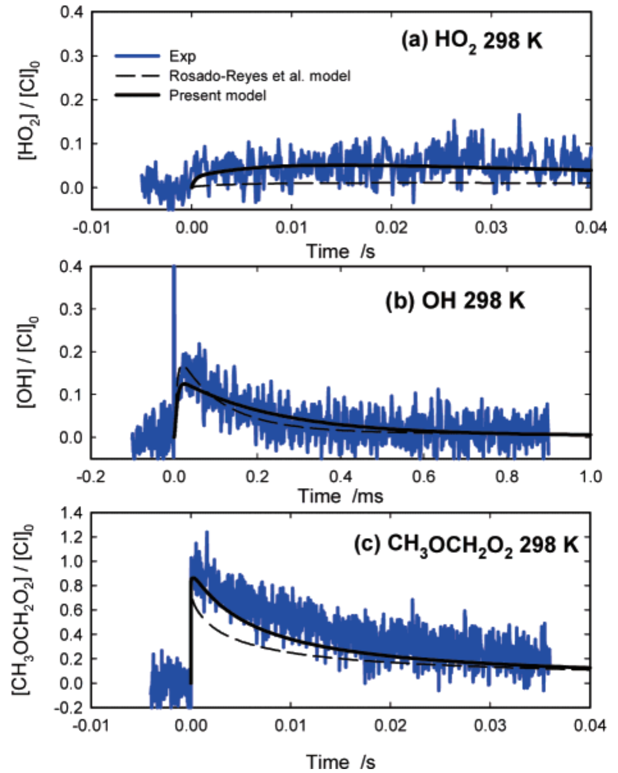

Figure 11. Scaled time profiles relative to initial chlorine atom concentration at 298 K. Bold line are calculated profiles using our model shown in Table 2, the dot-dash lines are the Rosado-Reyes et al. model.[38]

To predict the HO_2 and $CH_3OCH_2O_2$ experimental profiles, the direct formation of HCO (reaction 24), the direct formation of OH (reaction 22) and OH + $CH_3OCH_2O_2$ reactions (reaction 23) were also considered in this study. The reaction 23 is assumed to be temperature independent. The rate constants of reactions 29−31 were adopted from the values of the Rosado-Reyes et al. measurements. The rate constants of reactions 22 and 24 were determined by fitting to the experimental profiles as $k_{22} = 1.0 \times 10^{-12}$, and $k_{24} = 3.0 \times 10^{-14}$ cm^3 molecule^{-1} s^{-1} keeping the rate constant of the recombination reaction of $CH_3OCH_2 + O_2$ reaction (reaction 9) as it is. The branching ratio among reactions 9, 22, and 24 is 0.86:0.13:0.01. The initial rapid HO_2 formation is approximately 80% via OH + $CH_3OCH_2O_2$ and at most 10% via HCO. The slow HO_2 formation after 2 ms, balancing with the consumption, is via the series of reaction governed by $CH_3OCH_2O_2$ self-reaction.

UV Cross Section of $CH_3OCH_2O_2$. According to the analysis of HO_2 formation at 298 K and 34 Torr, the amount of $CH_3OCH_2O_2$ is 86% relative to the initial Cl concentration and the remaining 14% reach fission products without stabilization. The pressure dependence of the branching is shown in Figure 6. For the previous cross sections measured,[74] 100% of the Cl was assumed to convert to $CH_3OCH_2O_2$ at 298 K and 100 Torr. Figure 6 states that the $CH_3OCH_2O_2$ yield should be 90% at 100 Torr and 298 K. $CH_3OCH_2O_2$ is overestimated by about 10% by this factor. Our separate estimate of the $CH_3OCH_2O_2$ cross section considering this effect is shown in Figure 3, which is larger than the previous one by a factor of 1.2.

D. Model Evaluation. The CH_3OCH_3 oxidation model is constructed by combining the 600 and 298 K HO_2 formation mechanisms, as shown in Table 2. The rate constants of OH

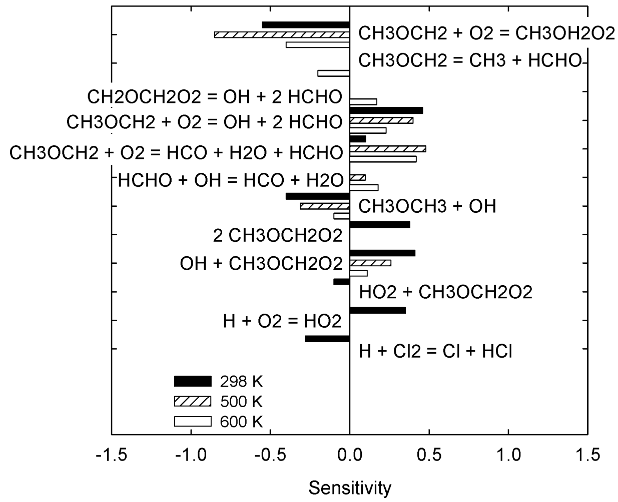

Figure 12. Sensitivity for HO_2 at 2 ms after photolysis at 298, 500, and 600 K.

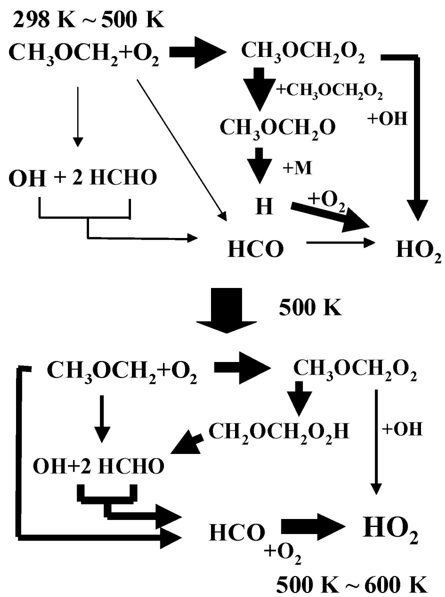

Figure 13. Schematic representation of HO_2 formation pathways at the temperature of 298 and 600 K in the Cl atom initiated oxidation of CH_3OCH_3.

direct formation and HCO direct formation from $CH_3OCH_2 + O_2$ reactions are determined to be $k_{22} = 1.55 \times 10^{-13} \times \exp(4.7\ \text{kJ/mol}/RT)$, and $k_{24} = 1.1 \times 10^{-13} \times \exp(-3.2\ \text{kJ/mol}/RT)$ cm^3 molecule^{-1} s^{-1} between 298 and 600 K. The temperature dependence of the yield is successfully predicted by this mechanism, as shown in Figure 6. Pressure dependence of the yield is also represented with this model, which supports the current mechanism that the pressure dependent stabilization of $CH_3OCH_2O_2$ competes with the direct formation of bimolecular products.

Sensitivity coefficients for HO_2 concentration 2 ms after the photolysis are shown in Figure 12. At 298 K, the direct formation of OH and HCO from $CH_3OCH_2 + O_2$ and $CH_3OCH_2O_2$ self-reaction are important for HO_2 formation. The OH + $CH_3OCH_2O_2$ reaction also has a large sensitivity for HO_2, which particularly contributes to the rapid HO_2 formation. The H + O_2 recombination reaction has a positive sensitivity because it competes with the H + Cl_2 reaction, whereas H production through reaction 29 is the essential point of this pathway. The HO_2 formation is governed by $CH_3OCH_2O_2$ self-reaction. This is the unique feature of CH_3OCH_3 oxidation. In the case of C_2 and C_3 alkanes, the RO_2 self-reaction is slower than $CH_3OCH_2O_2$ self-reaction by a factor of 10,[46] and the RO decomposition reaction is negligibly slow.[75] At 600 K, the direct formation of OH and HCO also has large sensitivity for HO_2, which particularly contributes to the rapid HO_2 formation. As the $CH_3OCH_2O_2$ isomerization effectively occurs under this condition, the $CH_2OCH_2O_2H$ decomposition reaction and HCHO + OH reaction largely contributes to HO_2 formation. OH + CH_3OCH_3 shows negative sensitivity, which competes with OH + HCHO, forming HO_2 via HCO + O_2 reaction. The OH + $CH_3OCH_2O_2$ reaction still has positive sensitivity. Also shown in the figure are coefficients at 500 K, where the HO_2 yield begins to increase sharply. The direct formation of HCO and OH from $CH_3OCH_2 + O_2$, and OH + $CH_3OCH_2O_2$ have positive sensitivity, whereas the recombination reaction of $CH_3OCH_2 + O_2$ has negative sensitivity. Other reactions that contribute to HO_2 formation at 298 and 600 K do not have significant sensitivity coefficients at 500 K. These results indicate that 500 K is the junction of the HO_2 mechanism in the reaction of $CH_3OCH_2 + O_2$. A schematic summary of the pathway toward HO_2 is shown in Figure 13.

Conclusions

The product branching between OH and HO_2 elimination channels in alkyl + O_2 reactions is the point that characterize the fuel specific low-temperature combustion property. From this standpoint, the time-resolved HO_2 and OH measurements were conducted in this system of Cl atom-initiated dimethyl ether oxidation. The detection of OH through the whole temperature range was direct proof of the dominant OH + 2HCHO exit channel from $CH_3OCH_2 + O_2$, which was predicted from the past indirect experimental evidence and theoretical considerations. On the other hand, the analysis of the HO_2 formation pathway was not straightforward, although the temperature-dependent yield and the formation profiles consisting of fast and slow components are phenomenologically similar to the cases of C2 and C3 alkanes. The presence of active OH, which readily reacts with the reactant and intermediates, made the system complex, so that we needed to add the function of UV absorption for further examination. In order to account for the OH, HO_2 and $CH_3OCH_2O_2$ observations in this range of temperature and pressure, existing mechanisms for high and low-temperature sides were individually modified. It has been revealed that the HO_2 formation is dominated by $CH_3OCH_2O_2$ self-reaction and OH + $CH_3OCH_2O_2$ below 500 K, whereas HCO + O_2 and HCHO + OH, both of which are formed promptly and slowly, dominates over 500 K. Among the reactions added and modified in this work, the HCO formation from QOOH species via the HOQO intermediate is a proposal that was not considered in any previous investigations, but supported by our own ab initio calculations. The HOQO route contributes partially throughout the temperature range. This HO_2 formation pathway is unique to this DME system, compared to the cases of small hydrocarbons for which HO_2 formation has already been studied. The independent measurement of CH_3OCH_2 thermal decomposition in the current pressure range could reduce the uncertainty of the model on the high-temperature side.

Acknowledgment. This study was supported by the Ministry of Education, Science, Sports, and Culture (MEXT), a Grant-in-Aid for Exploratory Research, 18360098, 2006. K.S. was supported through the 21st Century COE program, “Mechanical

System Innovation," by the Ministry of Education, Culture, Sports, Science, and Technology.

References and Notes

(1) Epping, K.; Aceves, S.; Bechtold, R.; and Dec, J. SAE Technical Paper **2002**-01-1923.

(2) Walker, R. W.; Morley, C. Basic Chemistry in Combustion. In *Low-Temperature Combustion and Autoignition*; Pilling, M. J., Ed.; Elsevier: Amsterdam, 1997; p 1.

(3) Westbrook, C. K. *Proc. Combust. Inst.* **2000**, *28*, 1563−1577.

(4) Miller, J. A.; Pilling, M. J.; Troe, J. *Proc. Combust. Inst.* **2005**, *30*, 43.

(5) Atkinson, R. *Atmos. Environ.* **2000**, *34*, 2063.

(6) Miller, J. A.; Klippenstein, S. J.; Robertson, S. H. *Proc. Combust. Inst.* **2000**, *28*, 1479.

(7) Clifford, E. P.; Farrell, J. T.; DeSain, J. D.; Taatjes, C. A. *J. Phys. Chem. A* **2000**, *104*, 11549.

(8) DeSain, J. D.; Clifford, E. P.; Taatjes, C. A. *J. Phys. Chem. A* **2001**, *105*, 3205−3213.

(9) DeSain, J. D.; Taatjes, C. A. *J. Phys. Chem. A* **2001**, *105*, 6646−6654.

(10) DeSain, J. D.; Taatjes, C. A.; Miller, J. M.; Klippenstein, S. J.; Hahn, D. K. *Faraday Discuss.* **2001**, *119*, 101−120.

(11) DeSain, J. D.; Klippenstein, S. J.; Taatjes, C. A. *Phys. Chem. Chem. Phys.* **2003**, *5*, 1584.

(12) DeSain, J. D.; Klippenstein, S. J.; Taatjes, C. A. *J. Phys. Chem. A* **2003**, *107*, 1992.

(13) DeSain, J. D.; Klippenstein, S. J.; Miller, J. A.; Taatjes, C. A. *J. Phys. Chem. A* **2003**, *107*, 4415.

(14) Estupián, E. G.; Klippenstein, S. J.; Taatjes, C. A. *J. Phys. Chem. B* **2005**, *109*, 8374.

(15) Taatjes, C. A. *J. Phys. Chem. A* **2006**, *110*, 4299.

(16) Sun, H.; Bozzelli, J. W. *J. Phys. Chem. A* **2004**, *108*, 1694.

(17) Dagaut, P.; Boettner, J. C.; Cathonnet, M. *Proc. Combust. Inst.* **1996**, *26*, 627.

(18) Pfahl, U.; Fieweger, K.; Adomeit, G. *Proc. Combust. Inst.* **1996**, *26*, 781.

(19) Curran, H. J.; Pitz, W. J.; Westbrook, C. K.; Dagaut, P.; Boettner, J. C.; Cathonnet, M. *Int. J. Chem. Kinet.* **1998**, *30*, 229.

(20) Dagaut, P.; Daly, C.; Simmie, J. M.; Cathonnet, M. *Proc. Combust. Inst.* **1998**, *27*, 361.

(21) Fischer, S. L.; Dryer, F. L.; Curran, H. J. *Int. J. Chem. Kinet.* **2000**, *32*, 713.

(22) Curran, H. J.; Fischer, S. L.; Dryer, F. L. *Int. J. Chem. Kinet.* **2000**, *32*, 741.

(23) Kaiser, E. W.; Wallington, T. J.; Hurley, M. D.; Platz, J.; Curran, H. J.; Pitz, W. J.; Westbrook, C. K. *J. Phys. Chem. A* **2000**, *104*, 8194.

(24) Liu, I.; Cant, N. W.; Bromly, J. H.; Barnes, F. J.; Nelson, P. F.; Haynes, B. S. *Chemosphere* **2001**, *42*, 583.

(25) Daly, C. A.; Simmie, J. M.; Wurmel, J. *Combust. Flame* **2001**, *125*, 1329.

(26) Zheng, X. L.; Lu, T. F.; Law, C. K.; Westbrook, C. K.; Curran, H. J. *Proc. Combust. Inst.* **2005**, *30*, 1101.

(27) Qin, X.; Ju, Y. *Proc. Combust. Inst.* **2005**, *30*, 233.

(28) Ju, Y.; Xue, Y. *Proc. Combust. Inst.* **2005**, *30*, 295.

(29) Cool, T. A.; Wang, J.; Hansen, N.; Westmoreland, P. R.; Dryer, F. L.; Zhao, Z.; Kazakov, A.; Kasper, T.; Kohse-Hoinghaus, K. *Proc. Combust. Inst.*, in press.

(30) Masaki, A.; Tsunashima, S.; Washida, N. *J. Phys. Chem.* **1995**, *99*, 13126.

(31) Hoyermann, K.; Nacke, F. *Proc. Comb. Inst.* **1996**, *26*, 505.

(32) Sehested, J.; Mogelberg, T.; Wallington, T. J.; Kaiser, E.; Nielsen, O. J. *J. Phys. Chem.* **1996**, *100*, 17218.

(33) Sehested, J.; Sehested, K.; Platz, J.; Egsgaard, H.; Nielsen, O. J. *Int. J. Chem. Kinet.* **1997**, *29*, 627.

(34) Maricq, M. M.; Szente, J. J.; Hybl, J. D. *J. Phys. Chem. A* **1997**, *101*, 5155.

(35) Yamada, T.; Bozzelli, J. W.; Lay, T. H. *Int. J. Chem. Kinet.* **2000**, *30*, 435.

(36) Anderson, A.; Carter, E. A. *Isr. J. Chem.* **2002**, *42*, 245.

(37) Anderson, A.; Carter, E. A. *J. Phys. Chem. A* **2003**, *107*, 9463.

(38) Rosado-Reyes, C. M.; Francisco, J. S.; Szene, J. J.; Maricq, M. M.; Ostergaard, L. F. *J. Phys. Chem. A.* **2005**, *109*, 10940.

(39) Suzaki, K.; Kanno, N.; Tonokura, K.; Koshi, M.; Tsuchiya, K.; Tezaki, A. *Chem. Phys. Lett.* **2006**, *425*, 179.

(40) Suzaki, K.; Chinzei, T.; Tsuchiya, K.; Koshi, M.; Tezaki, A. *Proc. Combust. Inst.*, in press.

(41) Taatjes, C. A.; Oh, D. B. *Appl. Opt.* **1997**, *36*, 5817.

(42) Kanno, N.; Tonokura, K.; Tezaki, A.; Koshi, M. *J. Mol. Spectrosc.* **2005**, *229*, 193.

(43) Fink, E. H.; Ramsay, D. A. *J. Mol. Spectrosc.* **1997**, *185*, 304.

(44) Fink, E. H.; Ramsay, D. A. *J. Mol. Spectrosc.* **2002**, *216*, 322.

(45) Abrams, M. C.; Davis, S. P.; Rao, L. P.; Engleman, R., Jr.; Brault, J. W. *Astrophys. J. Suppl. Ser.* **1994**, *93*, 351.

(46) Wallington, T. J.; Dagaut, P.; Kurylo, M. J. *Chem. Rev.* **1992**, *92*, 667.

(47) Langer, S.; Ljungstrom, E.; Ellermann, T.; Nielsen, O. J.; Sehested, J. *Chem. Phys. Lett.* **1995**, *240*, 53.

(48) Atkinson, R.; Baulch, D. L.; Cox, R. A.; Hampson, R. F., Jr.; Kerr, J. A.; Rossi, M. J.; Troe, J. *J. Phys. Chem. Ref. Data* **1997**, *26*, 521.

(49) Grotheer, H.; Riekert, G.; Walter, D.; Just, Th. *J. Phys. Chem.* **1988**, *92*, 4028.

(50) DeMore, W. B.; Howard, C. J.; Golden, D. M.; Kolb, C. E.; Hampson, R. F.; Molina, M. J. *Chemical Kintetics and Photochemical Data for Use in Stratospheric Modeling*; JPL Publication 97-4; Jet Propulsion Laboratory: Pasadena, CA, 1997.

(51) Miller, J. A.; Melius, C. F. *Combust. Flame.* **1992**, *91*, 21.

(52) Hippler, H.; Troe, J.; Willner, J. *J. Chem. Phys.* **1990**, *93*, 1755.

(53) Baulch, D. L.; Cobos, C. J.; Cox, R. A.; Frank, P.; Hayman, G.; Just, Th.; Kerr, J. A.; Murrells, T.; Pilling, M. J.; Troe, J.; Walker, R. W.; Warnatz, J. *J. Phys. Chem. Ref. Data* **1994**, *23*, 847.

(54) Li, S. C.; Williams, F. A. *Proc. Combust. Inst.* **1996**, *26*, 1017.

(55) Forster, R.; Frost, M.; Fulle, D.; Hamann, H. F.; Hippler, H.; Schlepegrell, A.; Troe, J. *J. Chem. Phys.* **1995**, *103*, 2949−2958.

(56) Atkinson, R.; Baulch, D. L.; Cox, R. A.; Hampson, R. F.; Kerr, J. A.; Rossi, M. J.; Troe, J. *J. Phys. Chem. Ref. Data* **1997**, *26*, 1329.

(57) Marinov, N. M.; Westbrook, C. K.; Pitz, W. J. *Transport Phenom. Combust.* **1995**, 118.

(58) Tsang, W.; Hampson, R. F. *J. Phys. Chem. Ref. Data* **1986**, *15*, 1087.

(59) Tsang, W.; Herron, J. T. *J. Phys. Chem. Ref. Data* **1991**, *20*, 609.

(60) Timonen, R. *Ann. Acad. Sci. Fenn. Ser. A2.* **1988**, *218*, 5.

(61) Pagsberg, P.; Munk, J.; Anastasi, C.; Simpson, V. J. *J. Phys. Chem.* **1989**, *93*, 5162.

(62) Michael, J. V.; Nava, D. F.; Payne, W. A.; Stief, L. J. *J. Chem. Phys.* **1979**, *70*, 3652.

(63) Loucks, L. F.; Laidler, K. J. *Can. J. Chem.* **1967**, *45*, 2767.

(64) Baulch, D. L.; Cobos, C. J.; Cox, R. A.; Esser, C.; Frank, P.; Just, Th.; Kerr, J. A.; Pilling, M. J.; Troe, J.; Walker, R. W.; Warnatz, J. *J. Phys. Chem. Ref. Data* **1992**, *21*, 411.

(65) Biggs, P.; Canosa-Mas, C. E.; Shallcross, D. E.; Vipond, A.; Wayne, R. P. *J. Chem. Soc., Faraday. Trans.* **1997**, *93*, 2701.

(66) Atkinson, R.; Baulch, D. L.; Cox, R. A.; Crowley, J. N.; Hampson, R. F., Jr.; Kerr, J. A.; Rossi, M. J.; Troe, J. *Summary of Evaluated Kinetic and Photochemical Data for Atmospheric Chemistry*; IUPAC Subcommittee on Gas Kinetic Data Evaluation for Atmospheric Chemistry Web Version, IUPAC: United Kingdom, 2001; pp 1−56.

(67) Mueller, M. A.; Kim, T. J.; Yetter, R. A.; Dryer, F. L. *Int. J. Chem. Kinet.* **1999**, *31*, 113.

(68) Baulch, D. L.; Duxbury, J.; Grant, S. J.; Motague, D. C. *J. Phys. Chem. Ref. Data* **1981**, *10*, Suppl.

(69) Mebel, A. M.; Morokuma, K.; Lin, M. C. *J. Chem. Phys.* **1995**, *103*, 7414.

(70) Gaussian 98, Revision A. 7, Frisch, M. J.; Trucks, G. W.; Schlegel, H. B.; Scuseria, G. E.; Robb, M. A.; Cheeseman, J. R.; Zakrzewisk, V. G.; Montgomery, J. A.; Saratmann, R. E.; Burant, J. C.; Dapprich, S.; Millam, J. M.; Daniels, A. D.; Kudin, K. N.; Strain, M. C.; Farkas, O.; Tomasi, J.; Barone, V.; Cossi, M.; Cammi, R.; Mennucci, B.; Pomelli, C.; Adamo, C.; Clifford, S.; Ochterski, J.; Petersson, G. A.; Ayala, P. Y.; Cui, Q.; Morokuma, K.; Malick, D. K.; Rabuck, A. D.; Raghavachari, K.; Foresman, J. B.; Cioslowski, J.; Ortiz, J. V.; Baboul, A. G.; Stefanov, B. B.; Lin, G.; Liashenko, A.; Piskorz, P.; Komaroni, I.; Gomperts, R.; Martin, R. L.; Fox, D. J.; Keith, T.; Al-Laham, M. A.; Peng, C. Y.; Nanayakkara, A.; Gonzalez, C.; Challacombe, M.; Gill, P. M. W.; Johnson, B.; Chen, W.; Wong, M. W.; Andres, J. L.; Gonzalez, C.; Head-Gordon, M.; Replogle, E. S.; and Pople, J. L. Gaussian, Inc.: Pittsburgh, PA, 1998.

(71) Gaussian 03, Revision B. 04, Frish, M. J.; Truck, G. W.; Schlegel, H. B.; Scuseria, G. E.; Robb, M. A.; Cheeseman, J. R.; Montgomery, J. A.; Verven, T.; Kudin, K. N.; Burant, J. C.; Millam, J. M.; Iyenger, S. S.; Tomasi, J.; Baroe, V.; Mennucci, B.; Cossi, M.; Scalmani, G.; Rega, N.; Petersson, G. A.; Nakatsuji, H.; Hada, M.; Ehara, M.; Toyota, K.; Fukuda, R.; Hasegawa, J.; Ishida, M.; Nakajima, T.; Honda, Y.; Kitao, O.; Nakai, H.; Klene, M.; Li, X.; Knox, J. E.; Hratchian, H. P.; Cross, J. B.; Adamo, C.; Jaramillo, J.; Gomperts, R.; Stratmann, R. E.; Yazyev, O.; Austin, A. J.; Cammi, R.; Pomelli, C.; Ochterski, J. W.; Ayala, P. Y.; Morokuma, K.; Voth, G. A.; Salvador, P.; Dannenberg, J. J.; Zakrzewski, V. G.; Dapprich, S.; Daniels, A. D.; Strain, M. C.; Farkas, O.; Malick, D. K.; Rabuck, A. D.; Raghavachari, K.; Foresman, J. B.; Ortiz, J. V.; Cui, Q.; Baboul, A. G.; Cliford, S.; Cioslowski, J.; Stefanov, B. B.; Liu, G.; Liashenko, A.; Piskorz, P.; Komaromi, I.; Martin, R. L.; Fow, D. J.; Keith, T.; Al-Laham, M. A.; Peng, C. Y.; Nanayakkara, A.; Challacombe, M.; Gill, P. M. w.; Johnson, B.; Chem ,W.; Wong, M. W.; Gonzalez, C.; Pople, J. A. Gaussian, Inc.: Pittburgh, PA, 2003.

(72) GAMESS VERSION = 22 FEB 2006 (R2) from Iowa State University. Schmidt, M. W.; Baldricidge, K. K.; Boatz, J. A.; Elbert, S. T.; Gordon, M. S.; Jensen, J. H.; Koseki, S.; Matsunaga, N.; Nguyen, K. A.; Su, S. J.; Windus, T. L.; Dupuis, M.; Montogomery, J. A. *J. Comput. Chem.* **1993**, *14*, 1347.

(73) Jenkin, M. E.; Hayman, G. D.; Wallington, T. J.; Hurley, M. D.; Ball, J. C.; Nielsen, O. J.; Ellermann, T. *J. Phys. Chem.* **1993**, *97*, 11712.

(74) Dagaut, P.; Wallington, T. J.; Kurylo, M. J. *J. Photochem. Photobiol. A. Chem.* **1989**, *48*, 187.

(75) Heicklen, J. *Adv. Photochem.* **1988**, *14*, 177.